An improved flux density distribution model for a flat heliostat (iHFLCAL) compared with HFLCAL

Caitou He[a], Yuhong Zhao[b,*], Jieqing Feng[a,*]

[a]*State Key Laboratory of CAD&CG, Zhejiang University, Hangzhou, 310058, China*
[b]*Institute of Industrial Process Control, College of Control Science and Engineering, Zhejiang University, Hangzhou, 310027, China*

Abstract

The simulation of the flux spot reflected by a flat heliostat is one of the fundamental problems in the central receiver system. In this paper, we propose an improved model based on Gaussian distribution assumption to more faithfully depict the flux density distribution on the receiver reflected by a flat heliostat, which is also the basis for study of the focusing heliostat. First, an imaginary flux density distribution is modeled by an elliptical Gaussian function in the image plane coordinate system. The relationship between the standard deviations of the Gaussian function and the heliostat length and width is revealed. Shading and blocking effects are carefully considered and addressed. Then, this distribution is mapped to the receiver plane through oblique parallel projection along the reflection direction of the heliostat based on the law of energy conservation and calculus. A state-of-the-art GPU-based ray tracing simulation method is adopted, and satisfactory consistency between the proposed model and the ray tracing result is found. The experiments and comparisons demonstrate that the proposed model is as efficient as but more accurate than the related Gaussian models.

Keywords: Flux density distribution, Elliptical Gaussian function, Oblique parallel projection, Ray tracing

1. Introduction

The solar thermal power tower plant, also called the central receiver system (CRS), is attracting worldwide attention as a renewable energy technology. The electricity generation efficiency and system operation safety are two major concerns in such a huge engineering project. Specifically, the thermal flux distribution on the receiver influences both the system efficiency and receiver lifetime, requiring intensive simulation of the flux density distribution on the receiver in advance. There are mainly two approaches to achieve the simulation goal, namely, the ray tracing method and the analytical method. In the classical ray tracing-based approach (Izygon et al., 2011), a sufficiently large quantity of rays has to be traced to obtain an accurate, reliable and stable result. The number of rays required is directly related to the heliostat size, heliostat-to-receiver distance, and heliostat microsurface slope error. According to our experiments, approximately 72 million rays are traced for a 3.2 m $\times$ 2.2 m heliostat, which is located 400 m from the receiver. This process takes 46 ms with a state-of-the-art GPU ray tracing simulation algorithm (Duan et al., 2019) implemented on a desktop PC equipped with an NVIDIA GeForce GTX 1080 GPU (Graphics Processing Units). By contrast, the analytical method outperforms the ray tracing method in terms of efficiency by calculating the flux value with an analytical expression directly.

Regarding the flux simulation problem, a flux density distribution model for the flux spot reflected by a flat heliostat is of significant importance. Two types of heliostats exist in CRS plants, i.e., flat and focusing he-

*Corresponding author
Email addresses: hctou89@zju.edu.cn (Caitou He), yhzhao@iipc.zju.edu.cn (Yuhong Zhao), jqfeng@cad.zju.edu.cn (Jieqing Feng)

liostats (including spherically or parabolically focusing heliostats) (Garcia et al., 2008). The latter is composed of well canted flat mirror facets. Thus, an accurate flux distribution model for the flat heliostat forms the basis to facilitate the composite focusing heliostat study (Chen et al., 2001). However, this task is complex because the flux spot is determined by many factors, including the sunlight direction, sun shape, and heliostat position, size, orientation and microheliostat surface slope error, among others. In addition, the shading and blocking effects are significant concerns that must be considered for accurate flux power prediction. In general, the analytical method approximates these effects in terms of a convolution. However, a closed-form solution to this convolution is a hard problem. Researchers have tried to solve the convolution via numerical approximation (Walzel et al., 1977) or via model simplification (Schmitz et al., 2006). The HFLCAL (short for Heliostat Field Layout CALculation) model (Schwarzbözl et al., 2009; García et al., 2015), which falls into the category of simplified models, is one of the most widely used analytical models with a simple and closed-form expression.

In this paper, we propose an improved model (iHFLCAL, "i" means "improved") as an improvement of the analytical models based on Gaussian distribution assumption to analytically describe the flat heliostat reflected flux spot on the receiver. First, an imaginary elliptical Gaussian function is established in the image plane coordinate system, taking shading and blocking effects into account and obeying the energy conservation principle. The relationships between the standard deviations of Gaussian function and the heliostat edges are established, thus the flux spots are better approximated. Second, the flux density result on the receiver plane is obtained by projecting the imaginary function onto the receiver plane through an oblique parallel projection. Abundant experiments and comparisons against a state-of-the-art ray tracing simulation approach, the HFLCAL related models and the state-of-the-art convolution-based Cauchy model (He et al., 2019) are conducted. The iHFLCAL model is demonstrated to be efficient and accurate.

The nomenclature used in this paper is as follows:

Nomenclature

- GPU Graphics Processing Units.
- HFLCAL Heliostat Field Layout CALculation.
- iHFLCAL improved HFLCAL.
- I_D sun direct normal irradiance (DNI).
- S_{eff} heliostat effective reflection surface area.
- η_{aa} atmospheric attenuation factor.
- d the distance between the heliostat and receiver.
- ρ heliostat reflectivity.
- σ standard deviation of Gaussian function.
- $\cos\theta$ heliostat incidence cosine efficiency.
- $\cos\phi$ receiver cosine efficiency.
- $\boldsymbol{r}$ reflection direction of the heliostat.
- $\boldsymbol{N}$ heliostat surface normal.
- $\boldsymbol{N}_r$ receiver panel normal.
- $\boldsymbol{c}$ receiver plane center.
- S_A microsurface area on the image plane.
- $S_{A'}$ area of the projected microsurface on the receiver plane.
- F_h flux density on the heliostat surface.
- F_{img} flux density on the image plane.
- F_{recv} flux density on the receiver plane.
- $\mathbf{I}$ the unitary matrix
- S_H total heliostat reflection surface area.
- P^r the flux power of ray tracing method.
- P^a the flux power of analytical model.
- ${F_{max}}^r$ the flux peak of ray tracing method.
- ${F_{max}}^a$ the flux peak of analytical model.
- e_{rms} root mean squared error.
- e_{power} the flux power error.
- e_{peak} the flux peak error.

The rest of the paper is organized as follows. Section 2 reviews the relevant work on analytical models for flux density distribution simulation, including the HFLCAL model and its variations. Section 3 elaborates the derivation of the model. Section 4 presents extensive experiments and comparisons with the related models and discusses the properties of the proposed model. Section 5 draws the conclusions and indicates planned future work.

2. Related work

2.1. Analytical flux simulation models

The analytical models place emphasis on fast simulations that essentially approximate the heliostat reflected flux spot on the receiver with a statistical function. In that function, multiple factors, including the sun parameters, heliostat parameters and atmospheric impact, are congregated in the form of convolution.

Biggs and Vittitoe (1976) numerically solved the convolution-based flux distribution expression through Fourier transformation. Walzel et al. (1977) adopted the 2D Hermite function to statistically simulate the flux density distribution on the receiver that is reflected by a flat heliostat. The computing time is cut down to a tenth of that of previous analytical models. Lipps and Walzel (1978) suggested a numerical method to calculate the flux density distribution of a heliostat of arbitrary shape, taking shading and blocking effects into account, which is more accurate but less efficient than the Hermite approximation approach. Hennet and Abatut (1984) established a complex analytical model based on the convolution between the solar disc and

the principle image of a heliostat on the rece iver. Shadowing effects were addressed by uniformly decreasing the flux power according to the proportion of heliostat effective reflection surface area. Collado et al. (1986) proposed the UNIZAR model in the integral form through image plane transition for a focusing heliostat, which is the convolution of several Gaussian error functions and is thus computationally expensive. He et al. (2019) proposed the convolution-based Cauchy model with a general and closed-form expression (Closed-form expression, 2019) to analytically model the flux distribution on the receiver, which can be directly evaluated. A model simplification may lead to a new solution, e.g., the HFLCAL model. Huang and Yu (2018) proposed to approximate the flux density distribution of a rectangular focusing heliostat with an elliptical Gaussian model but provided little discussion about the model parameters with the heliostat curving property.

2.2. Evolution of the HFLCAL model

The HFLCAL model was initially developed for fast annual power generation estimation of a well canted focusing heliostat and heliostat field layout optimization for a CRS (Schmitz et al., 2006). Schwarzbözl et al. (2009) published an overview of the original HFLCAL model, which had been acquired by the German Aerospace Center (DLR) in the early 1980s. In this model, the flux image reflected by each heliostat is modeled as a simple circular Gaussian distribution directly defined on the receiver plane, which is a comprehensive result of several distribution functions and justified by the central limit theorem (Schmitz et al., 2006). By calculating the integral of this distribution over the receiver plane, spillage loss is easily obtained, which is an important criterion for receiver tower height optimization for a specific heliostat field. Landman et al. (2016) added the effects of the solar beam incidence angle on the heliostat on the Gaussian distribution function. Since the standard deviation parameter "σ" of the Gaussian function is determined by other factors and is thus complex to analyze, Collado (2010) optimized "σ" according to the measured data by minimizing the flux peak difference with the ground truth, i.e., the one-point-fitting method. This model was then applied to heliostat aiming strategy optimization (Salomé et al., 2013; Besarati et al., 2014). García et al. (2015) refined the HFLCAL model and applied it to a flat heliostat by first modeling the reflected image as a circular normal distribution on the heliostat and then projecting the distribution to the receiver through homography transformation. This procedure produces a more accurate representation of the tilted flux spots reflected by most heliostats due to the oblique incidence of the reflected beam on the receiver. Shading and blocking effects were handled by including a factor which reduces the overall received power. He et al. (2017) proposed a novel rendering pipeline-based simulation framework developed on the GPU and achieved satisfactory efficiency with the refined HFLCAL model. Shading and blocking effects were better considered by the z-buffering algorithm; thus, the flux power was consistent with the ground truth.

3. Model analysis and derivation

A new model based on Gaussian assumption will be derived for the flux spot simulation on a receiver plane, with emphasis on the derivation of the flux density distribution equation and shading and blocking effects.

3.1. Overview of the model and the coordinate systems

For flux spot modeling purpose, all the heliostats are assumed to be precisely adjusted adopting the azimuth-elevation mode (Chen et al., 2004) to reflect the sunlight to the center of the receiver.

Four Cartesian coordinate systems (namely, the global coordinate system $\boldsymbol{O}$-$\boldsymbol{XYZ}$, the heliostat local coordinate system **o-st**, the image plane coordinate system $\boldsymbol{c}$-$\boldsymbol{xy}$ and the receiver plane coordinate system $\boldsymbol{c}$-$\boldsymbol{uv}$) are employed, as shown in Figure 1a. The global coordinate system $\boldsymbol{O}$-$\boldsymbol{XYZ}$ is left-handed, which is consistent with the graphics API (i.e., Direct3D) that we adopt. Its origin is at the tower base, and the $\boldsymbol{X}$-axis and $\boldsymbol{Z}$-axis point to the geographical east and north, respectively. In this paper, the azimuth of the sun is

defined clockwise from $\boldsymbol{X}$-axis in degrees, and the elevation is defined upwards from the horizon. The origin of the receiver plane coordinate system ***c-uv*** lies at the center of the receiver surface, and the $\boldsymbol{u}$-axis is parallel with the ground. The image plane coordinate system ***c-xy*** is perpendicular to the heliostat reflection direction $\boldsymbol{r}$, its $\boldsymbol{x}$-axis is parallel with the projection of the horizontal axis of the heliostat, and $\boldsymbol{y} = \boldsymbol{x} \times \boldsymbol{r}$.

The modeling process consists of two steps. First, an imaginary elliptical Gaussian function is established on the image plane, which is a virtual plane that passes the center of the receiver and is perpendicular to the reflection direction of the heliostat. Then, this function is projected to the receiver plane through an oblique parallel projection (Figure 1b). Thus, the flux density distribution on the receiver is obtained, and the distorted flux spot, i.e., typically of anisotropic elliptical Gaussian distribution pattern, is well described. The flux density distribution equation is deduced according to the energy conservation principle, geometrical relationships between the heliostat and the receiver, and calculus.

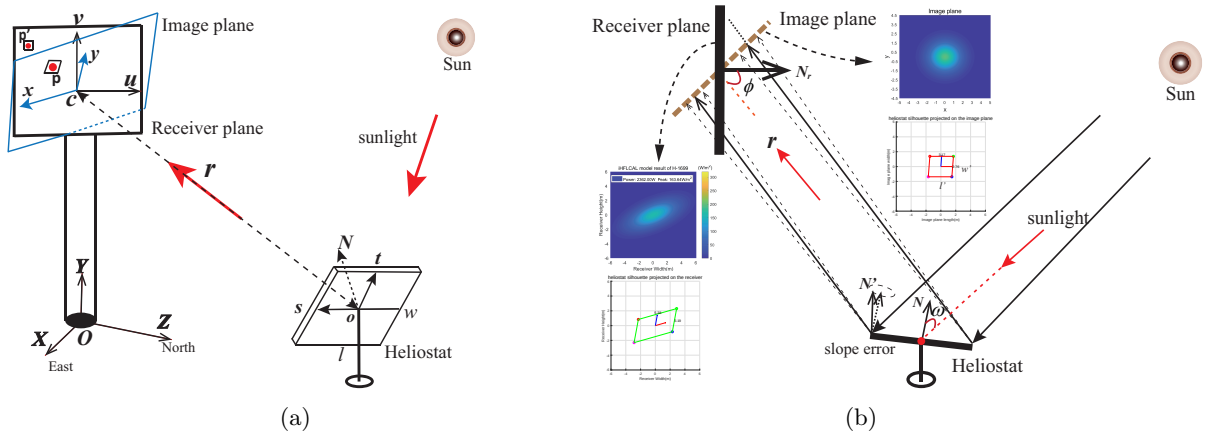

Figure 1: Overview of the model: (a) four coordinate systems (global coordinate system ***O-XYZ***, heliostat coordinate system **o-st**, image plane coordinate system ***c-xy*** and receiver plane coordinate system ***c-uv***) are adopted for the modeling purpose, and (b) the final flux spot on the receiver is the projection of an imaginary elliptical Gaussian distribution function defined in the image plane coordinate system, which is modeled according to the heliostat projection silhouette on the image plane.

3.2. Flux spot analysis

From a theoretical point of view, the flux spot on the receiver is influenced by many factors (Lovegrove and Stein, 2012), including the sunlight direction, sun shape, heliostat position, size, orientation, and microsurface slope errors, among others, as shown in the schematic drawing in Figure 1b. The sunlight beam reflected by the heliostat is scattered due to the imperfect reflection of the practical mirror surface, which is subjected to the heliostat slope error and commonly modeled as a Gaussian-distributed function in the hemisphere in front of the surface. In computer graphics, the Beckmann distribution model (Katzin, 1963; Cook, 1982) perfectly describes the reflectance of microfacets of the mirror, which is a physically based model and depicts the intensity distribution of the reflected light as a Gaussian pattern. The diffusion phenomenon of the reflected light beam becomes more evident as the mirror slope error or the distance between the heliostat to the receiver increases, in which the scattering effect caused by the heliostat microsurface and sun shape takes the dominant position relative to the heliostat size. On the other hand, according to the central limit theorem (Central limit theorem, 2018), the sum of these independent effects tends toward a normal distribution on a plane that is perpendicular to the reflection direction, i.e., the image plane, which is consistent with the ray tracing-based simulation statistical results. Finally, the proportion of the projected edges of the rectangular heliostat on the image plane should be considered (Figure 2). In summarize, it is more reasonable to first approximate the imaginary flux spot on the image plane with an elliptical Gaussian function and then map this spot to the receiver.

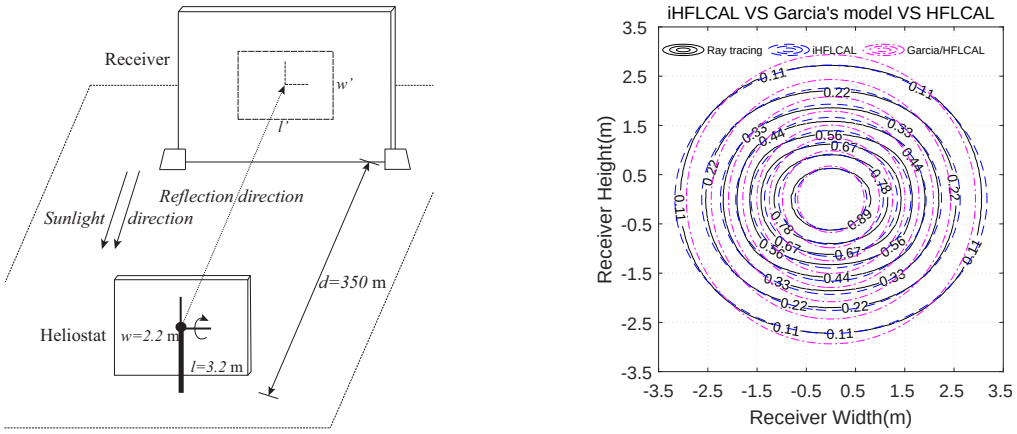

(a) (b)

Figure 2: The assumption of an elliptical Gaussian distribution pattern on the image plane is more reasonable than a circular Gauss to depict the flux spot reflected by a flat rectangular heliostat: (a) a rectangular flat heliostat reflects the sunlight to a vertically placed receiver; (b) comparison of the normalized flux density contours of the ray tracing result, the results based on elliptical Gaussian assumption and the circular Gaussian assumption (Schwarzbözl et al. (2009); García et al. (2015)).

3.3. Imaginary elliptical Gaussian flux density distribution on the image plane

In this part, we propose to model the imaginary flux density distribution on the image plane as an elliptical Gaussian function. This function takes shading and blocking effects into account and will later be projected onto the receiver along the reflection direction of the heliostat.

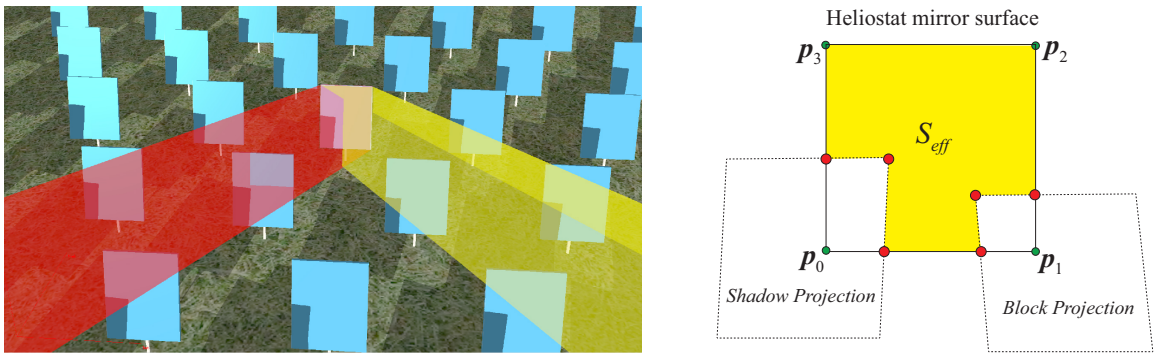

(a) (b)

Figure 3: (a) The incident sunlight beam (red parallelepiped) and reflected one (yellow parallelepiped) of a heliostat are occluded by the neighbor heliostats; (b) the shading and blocking objects are projected to the blocked heliostat, and the effective reflection surface (yellow area) is obtained with the Weiler-Atherton clipping algorithm.

To handle shading and blocking effects, a light beam traversal algorithm (He et al., 2017) is implemented to quickly determine the shading and blocking relationship for each heliostat in parallel on the GPU. Then, the shading and blocking heliostats are projected to the investigated heliostat along the sunlight direction and counter-reflected direction of the heliostat, respectively. Finally, the projections of the occluders are clipped off with the Weiler-Atherton algorithm (Weiler and Atherton, 1977), and the effective reflecting surface area S_{eff} (m^2) is obtained (Figure 3). Considering the shading and blocking effects, the reflected power of the investigated heliostat is calculated as

$$P_h = I_D \cdot S_{eff} \cdot cos\theta \cdot \rho, \tag{1}$$

where I_D is the solar DNI (W/m^2), θ is the angle (rad) between the sun direction and heliostat normal, and ρ is the heliostat reflectivity. That is, the reflected power is reduced in proportion to the shaded and blocked

area of the heliostat.

Based on the analysis in Section 3.2, the reflected flux density distribution on the image plane can be modeled as an elliptical Gaussian pattern. A normalized elliptical Gaussian function is expressed as

$$G(x,y) = \frac{1}{2\pi\sigma_1\sigma_2\sqrt{1-\gamma^2}} e^{-\frac{1}{2(1-\gamma^2)}[\frac{(x-\mu_1)^2}{\sigma_1^2} - 2\gamma\frac{(x-\mu_1)(y-\mu_2)}{2\sigma_1\sigma_2} + \frac{(y-\mu_2)^2}{\sigma_2^2}]}. \tag{2}$$

Since the flux spot center is the origin of the image plane coordinate system and the light beam scattering effects along the $\boldsymbol{x}$-axis and $\boldsymbol{y}$-axis are independent, so $\mu_1 = \mu_2 = 0, \gamma = 0$. Thus,

$$G(x,y) = \frac{1}{2\pi\sigma_1\sigma_2} e^{-\frac{1}{2}(\frac{x^2}{\sigma_1^2} + \frac{y^2}{\sigma_2^2})}. \tag{3}$$

According to the energy conservation principle and accounting for the atmosphere attenuation effect, the flux density ($\mathrm{W/m^2}$) of any point $\boldsymbol{p}(x,y)$ on the image plane is modeled as

$$F_{img}(\boldsymbol{p}) = F_{img}(x,y) = P_h \cdot \eta_{aa} \cdot G(x,y) = I_D \cdot S_{eff} \cdot cos\theta \cdot \rho \cdot \eta_{aa} \cdot \frac{1}{2\pi\sigma_1\sigma_2} e^{-\frac{1}{2}(\frac{x^2}{\sigma_1^2} + \frac{y^2}{\sigma_2^2})}, \tag{4}$$

where $\eta_{aa} \in (0,1)$ is the atmosphere attenuation factor, which can be calculated as a function of the distance d between the heliostat and the receiver by empirical models, e.g., the model proposed by Leary et al. (1979):

$$\eta_{aa} = \begin{cases} 0.99321 - 0.0001176 * d + 1.97 * 10^{-8} * d^2 & d \leq 1000 \text{ m} \\ e^{-0.0001106 * d} & d > 1000 \text{ m} \end{cases} \tag{5}$$

Theoretically, the standard deviations (σ_1 and σ_2) of the elliptical Gaussian function are closely related to the heliostat projection edges on the image plane (Figure 1b). An experiment has been conducted to determine the proportion of σ_1 to σ_2 empirically. That is, we aim to figure out a proper function $f(x)$:

$$\frac{\sigma_1}{\sigma_2} = f(\frac{l'}{w'}). \tag{6}$$

Four candidate elementary functions are considered, i.e., $\{f_1(x) = x, f_2(x) = \ln(x) + 1, f_3(x) = \sqrt{x}, f_4(x) = \log_{10}(x) + 1\}$. The trend of these functions in the range of $0.0 \sim 3.0$ are show in Figure 4.

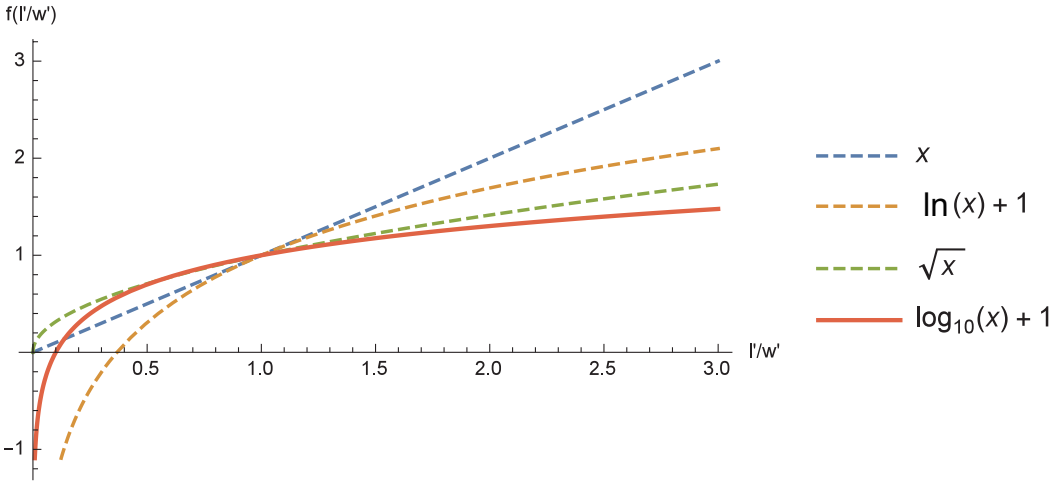

Figure 4: Curve visualization of four elementary functions.

According to the experiments, when $\frac{\sigma_1}{\sigma_2} = f_4(\frac{l'}{w'}) = 1 + \log_{10}\frac{l'}{w'}$, the elliptical Gaussian function achieves a

relatively better simulation results in terms of flux density distribution, which can be quantitatively measured by the normalized root mean squared error (e'_{rms}, (17)), as shown in Figure 5:

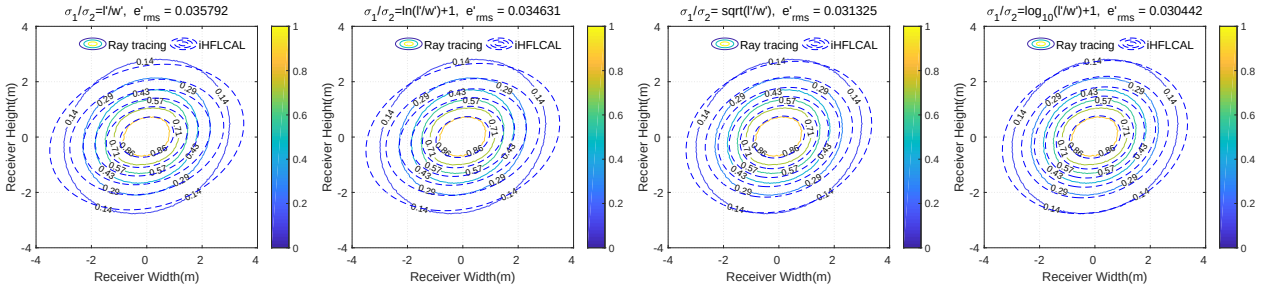

(a) $\frac{\sigma_1}{\sigma_2} = f_1(\frac{l'}{w'})$ (b) $\frac{\sigma_1}{\sigma_2} = f_2(\frac{l'}{w'})$ (c) $\frac{\sigma_1}{\sigma_2} = f_3(\frac{l'}{w'})$ (d) $\frac{\sigma_1}{\sigma_2} = f_4(\frac{l'}{w'})$

Figure 5: Comparison of the normalized flux density distribution results under four function relationship assumption.

So, we assume that

$$\frac{\sigma_1}{\sigma_2} = \beta = 1 + \log_{10}\frac{l'}{w'}. \tag{7}$$

Note that β can be analytically calculated based on the heliostat and receiver parameters.

Substituting (7) into (4) and replacing the symbol σ_1 with σ, we have

$$F_{img}(\boldsymbol{p}) = F_{img}(x,y) = P_h \cdot \eta_{aa} \cdot G(x,y) = I_D \cdot S_{eff} \cdot cos\theta \cdot \rho \cdot \eta_{aa} \cdot \frac{\beta}{2\pi\sigma^2} e^{-\frac{x^2+\beta^2 y^2}{2\sigma^2}}, \tag{8}$$

σ is the standard deviation of the Gaussian function approximating the comprehensive effect of the sun shape and various normal distributions (Schwarzbözl et al., 2009), e.g., beam quality (depicted by the heliostat slope error σ_s), and astigmatism error (σ_{ast}), among other effects (Schmitz et al., 2006; Collado, 2010; Besarati et al., 2014):

$$\sigma = \sqrt{d^2(\sigma_{sun}^2 + (2\sigma_s)^2 + \sigma_{ast}^2)} \tag{9}$$

d is the distance between the heliostat and receiver.

3.4. Flux projection from the image plane to the receiver plane

The imaginary flux density distribution defined on the image plane can be mapped to the receiver plane analytically. First, the receiver is discretized into grids. Second, the center of each receiver grid is projected to the image plane. Third, the relationship of the flux density of the point on the receiver and that of the corresponding point on the image plane is deduced mathematically. These procedures are processed on GPU in parallel for each receiver grid.

According to the ray-plane intersection equation, any point $\boldsymbol{p'} = (p'_x, p'_y, p'_z)^{\mathrm{T}}$ on the receiver plane can be projected to point $\boldsymbol{p} = (p_x, p_y, p_z)^{\mathrm{T}}$ on the image plane along the heliostat reflection direction through an oblique parallel projection:

$$\boldsymbol{p} = \mathbf{M}\boldsymbol{p'} + a\boldsymbol{r}, \tag{10}$$

in which

$$\mathbf{M} = \begin{bmatrix} 1 - r_x r_x & -r_y r_x & -r_z r_x \\ -r_x r_y & 1 - r_y r_y & -r_z r_y \\ -r_x r_z & -r_y r_z & 1 - r_z r_z \end{bmatrix} = \mathbf{I} - \boldsymbol{r}\boldsymbol{r}^{\mathrm{T}}, \tag{11}$$

where $\mathbf{I}$ is the unitary matrix, $\boldsymbol{r} = (r_x, r_y, r_z)^{\mathrm{T}}$ is the normalized reflection direction, $a = \boldsymbol{r} \cdot \boldsymbol{c}$, and $\boldsymbol{c}$ is the receiver plane center.

Then, the flux density relationship between $\boldsymbol{p}'$ and the projected point $\boldsymbol{p}$ on the image plane can be deduced using calculus. Suppose $\boldsymbol{p}$ is the central point of a microsurface (with area S_A) on the image plane (Figure 1a). The microsurface is sufficiently small that the flux density on it can be assumed to be constant. $S_{A'}$ is the area of the projection of this microsurface on the receiver plane under parallel projection along the reflection direction of the heliostat. According to the geometric relationship, we have

$$S_A = S_{A'} \cdot \cos\phi, \tag{12}$$

where ϕ is the angle between the heliostat reflection direction and the normal of the receiver plane. Equation (12) reveals the well-known receiver cosine effects. According to the energy conservation principle, we obtain

$$F_{recv}(\boldsymbol{p}') \cdot S_{A'} = F_{img}(\boldsymbol{p}) \cdot S_A, \tag{13}$$

in which $F_{recv}(\boldsymbol{p}')$ represents the flux density ($\mathrm{W/m^2}$) of point $\boldsymbol{p}'$ on the receiver.

Substituting (12) and (8) into (13), we obtain

$$F_{recv}(\boldsymbol{p}') = \frac{F_{img}(\boldsymbol{p}) \cdot S_A}{S_{A'}} = F_{img}(\boldsymbol{p}) \cdot cos\phi = I_D \cdot S_{eff} \cdot cos\theta \cdot \rho \cdot \eta_{aa} \cdot cos\phi \cdot \frac{\beta}{2\pi\sigma^2} e^{-\frac{x^2+\beta^2 y^2}{2\sigma^2}}. \tag{14}$$

Note that (x, y) is the coordinate of the corresponding point $\boldsymbol{p}$ in the image plane coordinate system, which can be calculated by (10) and coordinate transformation from 3D to 2D on the image plane:

$$\begin{cases} x = (\boldsymbol{p} - \boldsymbol{c}) \cdot \boldsymbol{i} \\ y = (\boldsymbol{p} - \boldsymbol{c}) \cdot \boldsymbol{j}, \end{cases} \tag{15}$$

$\boldsymbol{i}$ and $\boldsymbol{j}$ are the unit vector of the $\boldsymbol{x}$-axis and $\boldsymbol{y}$-axis of the image plane coordinate system.

3.5. Comparison with related models

Table 1: Comparison of flux density functions based on the Gaussian distribution assumption.

Models	flux density equation	Gaussian type	heliostat type	modeling process
Circular Gaussian model (Schwarzbözl et al., 2009)	$F_{recv}(u,v) = \frac{I_D \cdot S_H \cdot cos\theta \cdot \rho \cdot \eta_{aa}}{2\pi\sigma^2} e^{-\frac{u^2+v^2}{2\sigma^2}}$	circular	focusing	on the receiver
Refined HFLCAL (García et al., 2015)	$F_h(x,y) = \frac{I_D \cdot S_{eff} \cdot \rho \cdot \eta_{aa}}{2\pi\sigma^2} e^{-\frac{x^2+y^2}{2\sigma^2}}$	circular	focusing/flat	heliostat to receiver
Huang and Yu (2018)	$F_{img}(x,y) = \frac{I_D \cdot S_H}{2\pi D^2 \sigma_x \sigma_y} e^{-\frac{1}{2D^2}(\frac{x^2}{\sigma_x^2}+\frac{y^2}{\sigma_y^2})}$	elliptical	focusing	image to receiver
iHFLCAL model	$\beta = (1 + \log_{10}\frac{w'}{h'})$, $F_{img}(x,y) = \frac{\beta \cdot I_D \cdot S_{eff} \cdot cos\theta \cdot \rho \cdot \eta_{aa}}{2\pi\sigma^2} e^{-\frac{x^2+\beta^2 y^2}{2\sigma^2}}$	elliptical	flat	image to receiver

A comparison of the related models that based on the Gaussian distribution assumption is listed in Table 1. The symbols are consistent with the preceding definitions. $F_h(x,y)$, $F_{img}(x,y)$ and $F_{recv}(u,v)$ represent the flux density expression on the heliostat, image plane and receiver, respectively. The circular Gaussian model (Schwarzbözl et al., 2009) directly depicts the flux spot on the receiver with a circular Gaussian function, regardless of the heliostat shape and projection. The refined HFLCAL (García et al., 2015) model better approximates the tilted flux spots by introducing homography transformation from heliostat to the receiver plane, considering the shading and blocking effects. Huang and Yu (2018) modeled the flux spot reflected by a focusing heliostat with an elliptical Gaussian function on the image plane. Since the focusing heliostat is considered, two independent parameters (σ_1, σ_2) are required to be optimized to approximate the flux spots.

In our model, because the curvatures of the flat heliostat surface along the long and short edges are the same (equal 0), a single parameter is adequate and reasonable.

4. Experiments, comparisons and discussions

In this section, the accuracy and efficiency of the iHFLCAL model are demonstrated. The properties of the iHFLCAL model is discussed through experiments and comparisons with the ray tracing method (Duan et al., 2019) on a synthetic rectangular heliostat field. The accuracy of the iHFLCAL model is compared with the circular Gaussian model (Schwarzbözl et al., 2009), the refined HFLCAL model (García et al., 2015), and the convolution-based Cauchy model (He et al., 2019), which are all analytical models with closed-form expression. These models were implemented in a versatile GPU rendering-pipeline-based framework (He et al., 2017) on a desktop PC with an Intel core (TM) i5-3450 @3.10 GHz CPU and an NVIDIA GeForce GTX 1080 GPU.

Table 2: Two sun positions for the experiments and comparisons

	Altitude	Azimuth	DNI (W/m^2)
Early morning	9.5°	30.0°	681.0
Midday	80.2°	95.0°	1000.0

Table 3: Parameters of the heliostats used in the experiments and comparisons

Heliostat id	x (m)	y (m)	z (m)	d (m)	Length (m)	Width (m)	Reflectivity (ρ)
980	172.5	1.5	125.0	213.03	3.2	2.2	0.88
1960	97.5	1.5	175.0	200.33	3.2	2.2	0.88
2113	-132.5	1.5	185.0	227.56	2.5	2.5	0.88
2899	-182.5	1.5	225.0	289.71	3.2	2.2	0.88
3005	-150.0	1.5	250.0	291.55	2.0	2.0	0.88
4684	-212.5	1.5	335.0	396.72	2.0	2.0	0.88
5900	-102.5	1.5	395.0	408.09	2.0	2.0	0.88
6933	87.5	1.5	475.0	482.99	2.0	1.5	0.88
7875	-177.5	1.5	525.0	554.2	2.0	1.5	0.88

For illustration purpose, two representative cases of sun position (Table 2) were designed. One is in the early morning when the sun's altitude is low and the shading and blocking phenomena are common in the heliostat field. The other case is in the middle of the day. The synthesized experimental field (Figure 6) composes three regions with different sizes of flat heliostats (i.e., 3.2 m × 2.2 m, 2.0 m × 2.0 m, and 2.0 m × 1.5 m). In each region, the row distance and column distance equal to 5.0 m. Heliostats in the adjacent rows are elaborately staggered to alleviate the shading or blocking loss. The standard deviation of the heliostat slope error σ_s is assumed to be 2.0 mrad in the ray tracing method. Nine heliostats were sampled for experiments, whose parameters are listed in Table 3. (x,y,z) is the heliostat global coordinate, and d is its distance to the receiver. All the heliostats focus the sunlight at the center (0.0, 110.0, 0.5) of the receiver plane, which is 12 m × 12 m and faces geographical north.

The receiver plane is subdivided into uniform grids and the flux density of each grid is recorded. The resolution of the receiver grids in the ray tracing method and the analytical models are identically set as 5 × 5 cm^2/grid for a tradeoff between simulation accuracy and efficiency. Clearly, the flux power is the integration of the flux density distribution over the receiver domain. Apart from the flux peak, the flux density distribution and flux power received on the receiver are also important. Accordingly, three error metrics are adopted to

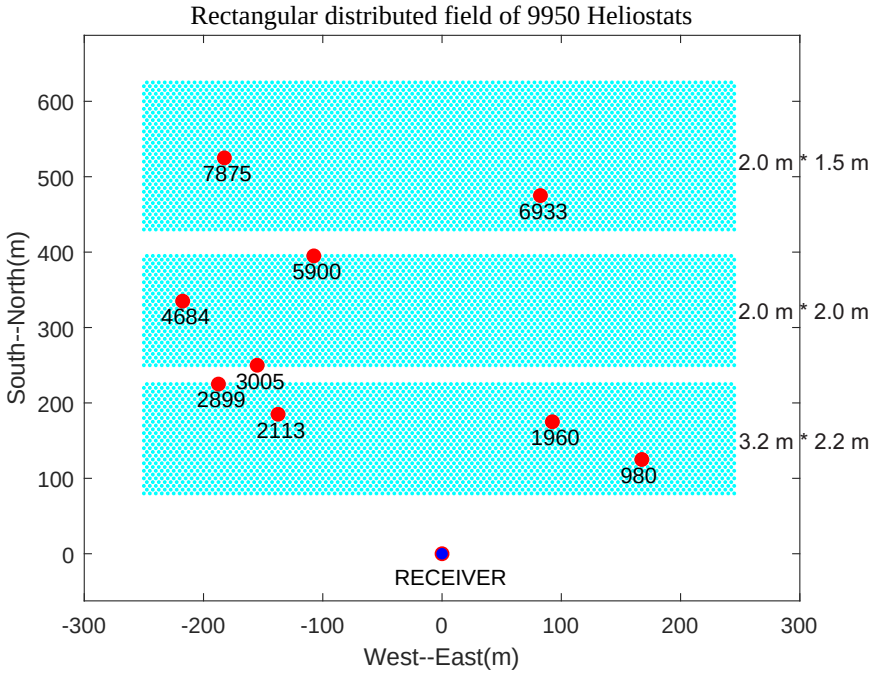

Figure 6: A rectangular staggered heliostat field is created. The heliostats being investigated are indicated with their indexes.

quantitatively evaluate the analytical models: the root mean squared error (e_{rms}), flux power error (e_{power}) and peak error (e_{peak}). These metrics are defined as follows:

$$e_{rms} = \sqrt{\frac{\sum_{i=1}^{N}({F_i}^a - {F_i}^r)^2}{N}}(\mathrm{W/m^2}), \quad e_{power} = \frac{||P^a - P^r||}{P^r}(\%), \quad e_{peak} = \frac{||F^a_{max} - F^r_{max}||}{F^r_{max}}(\%), \tag{16}$$

where N is the number of receiver surface tessellation grids, ${F_i}^a$ and ${F_i}^r$ stand for the flux density value predicted by the analytical method and the ray tracing method at the ith receiver grid, P^a and P^r are the flux power of the analytical model and the ray tracing method, F^a_{max} and F^r_{max} are the flux peak value of the analytical model and the ray tracing results, respectively. By the way, the normalized root mean squared error is defined as:

$$e'_{rms} = \sqrt{\frac{\sum_{i=1}^{N}({F_i}^a - {F_i}^r)^2}{N}}/F^r_{max} \tag{17}$$

4.1. Flux density distribution simulation results and comparisons

Figure 7 shows the flux density distribution simulated by the ray tracing method and the proposed iHFLCAL model, along with the visualization of the heliostat silhouette projection on the image plane and receiver surface. Note that the flux spots predicted by the iHFLCAL model are consistent with the ray tracing method, and their orientations are in accordance with heliostat projections on the receiver.

Figure 8 and Figure 9 present the comparisons of the iHFLCAL model with the related models that based on Gaussian distribution assumption in the midday and the early morning. The statistic results of three error metrics (i.e., e_{rms}, e_{power}, and e_{peak}) (16) of all the sampled heliostats are presented in Figure 10.

By comparing the flux density contour images and statistic results of these models, several conclusions can be reached. First, since the iHFLCAL model takes all the energy reduction factors into account, particularly the shading and blocking effects, the flux powers predicted by the iHFLCAL model are always consistent with the

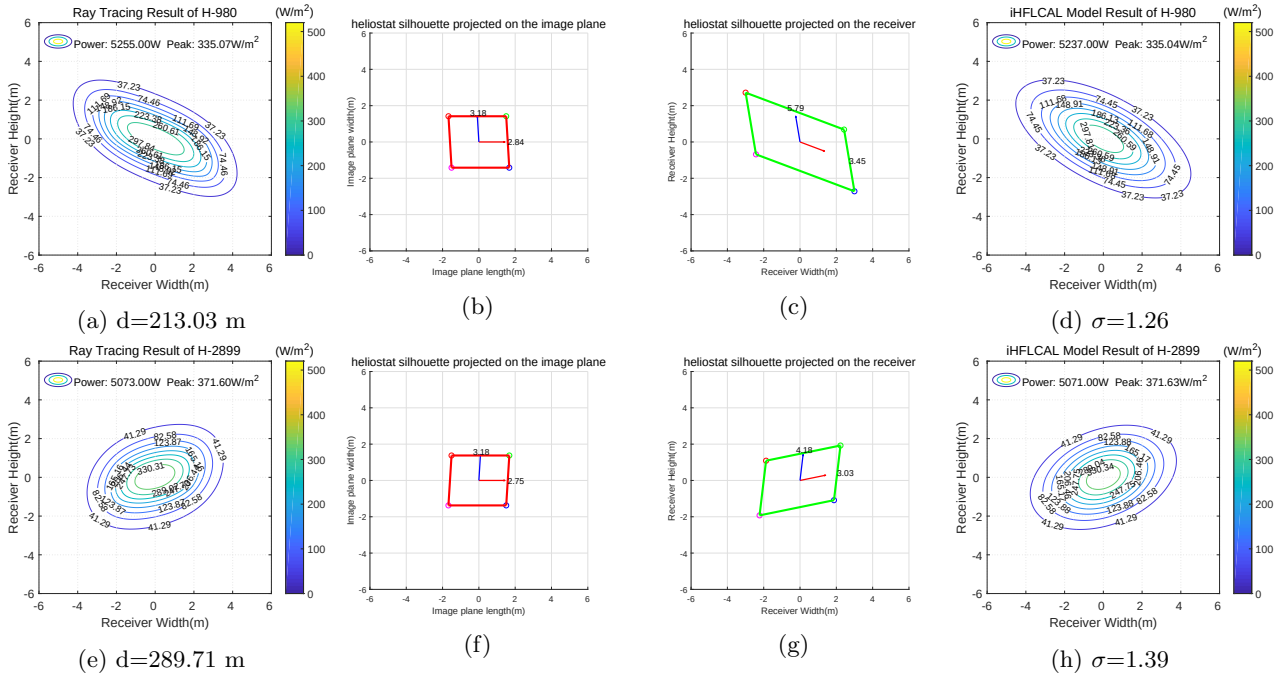

(a) d=213.03 m (b) (c) (d) σ=1.26

(e) d=289.71 m (f) (g) (h) σ=1.39

Figure 7: Flux spot predicted by the ray tracing method (1st column), heliostat silhouette projection on the image plane (2nd column) and on the receiver (3rd column), and the flux distribution result from the iHFLCAL model (4th column).

ray tracing results in both cases (Figure 10b;Figure 10e). By contrast, the circular Gaussian model work well in the midday case but overestimate the flux power when the heliostat is partially shaded or blocked in the early morning case. Second, the tilted flux spots on the receiver are more precisely approximated in the iHFLCAL model. This can be ascribed to the consideration of heliostat projection edges on the image plane. The principle axes of the flux spot predicted by the iHFLCAL model are consistent with the ground truth (obtained by the ray tracing method), while the other two models manifest deviations, particularly the circular Gaussian model, which is directly defined on the receiver plane without considering the heliostat reflected direction information. Third, the peak errors of all the three methods in both cases are negligible (less than 0.1%). Finally, the e_{rms} of the iHFLCAL model are smaller than or comparable to the other two models (Figure 10), indicating a more accurate representation of the flux spots. These results arise from the modeling process of the image plane to the receiver plane projection and the new flux density distribution equation. Furthermore, the root mean squared errors (e_{rms}) of the three models tend to converge to a relative low value (consistently, the flux spots are becoming analogous), as the heliostat-to-receiver distance increases. Theoretically, this is due to the fact that for the heliostats far from the receiver (more than 300 m in the present field), the effects of the heliostat geometry and position are concealed, and the sun shape and heliostat slope error take the dominant position.

4.2. Computational efficiency

Due to the simple and closed-form analytical expression of the iHFLCAL model, it is well suited for the GPU rendering-pipeline-based simulation framework (He et al., 2017) and achieves fast performance. In general, the calculation of the flux density distribution on the receiver (discrete grid resolution 2500 grids/m^2) needs approximately only 1.0 ms on the current machine. By contrast, the ray tracing method needs to trace a large number of rays to obtain an accurate and stable result. The bidirectional ray tracing method (Duan et al., 2019) was implemented, and 72 million rays were traced for the No. 2899 heliostat (3.2 m $\times$ 2.2 m), which is located 289.71 m from the receiver. The process took 46 ms in the same experimental environment.

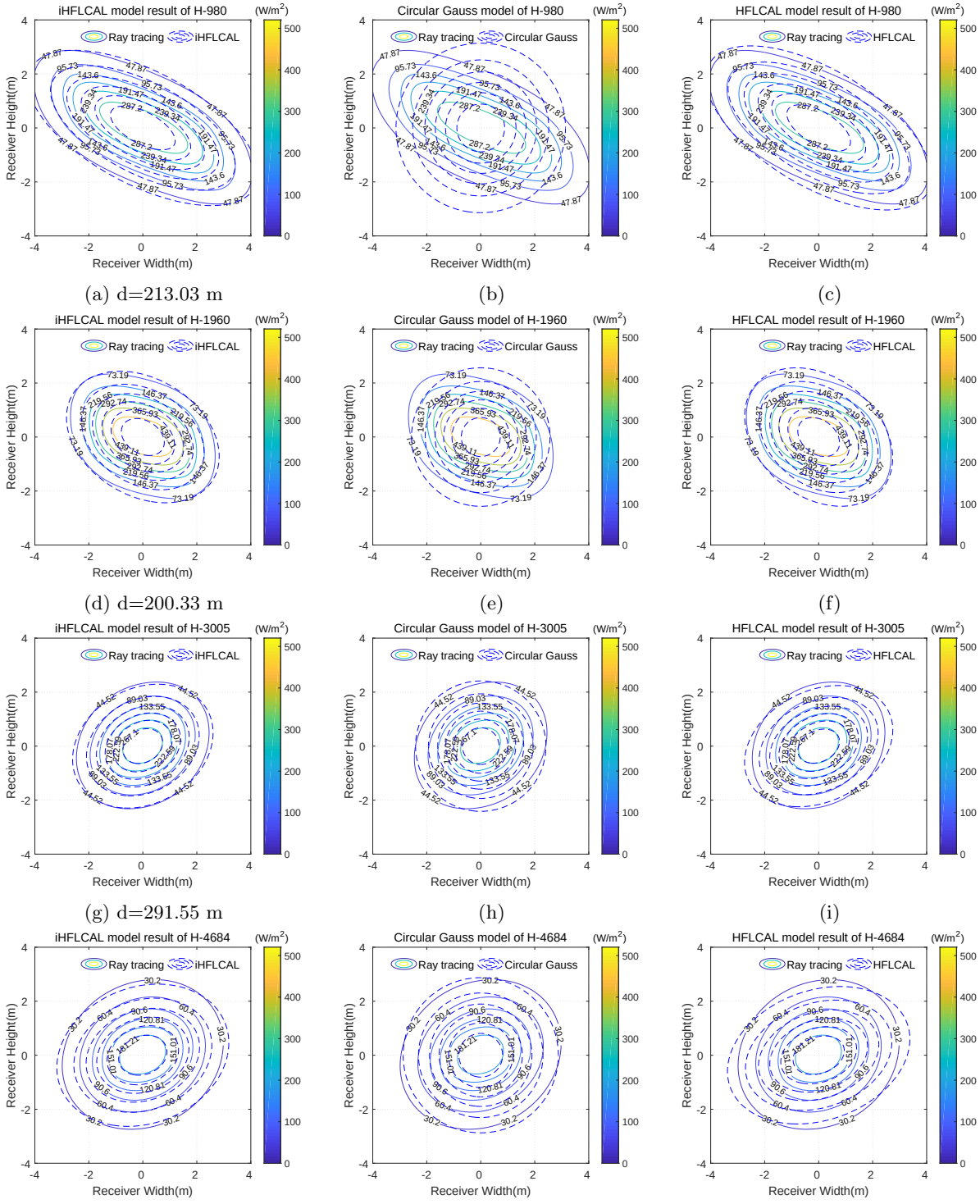

(a) d=213.03 m (b) (c)

(d) d=200.33 m (e) (f)

(g) d=291.55 m (h) (i)

(j) d=396.72 m (k) (l)

Figure 8: Comparison of the simulation results of the proposed iHFLCAL model (left column), the circular Gaussian model (middle column) and the refined HFLCAL model (right column) and in the midday case. The ray tracing simulation results (solid line) are regarded as the ground truth.

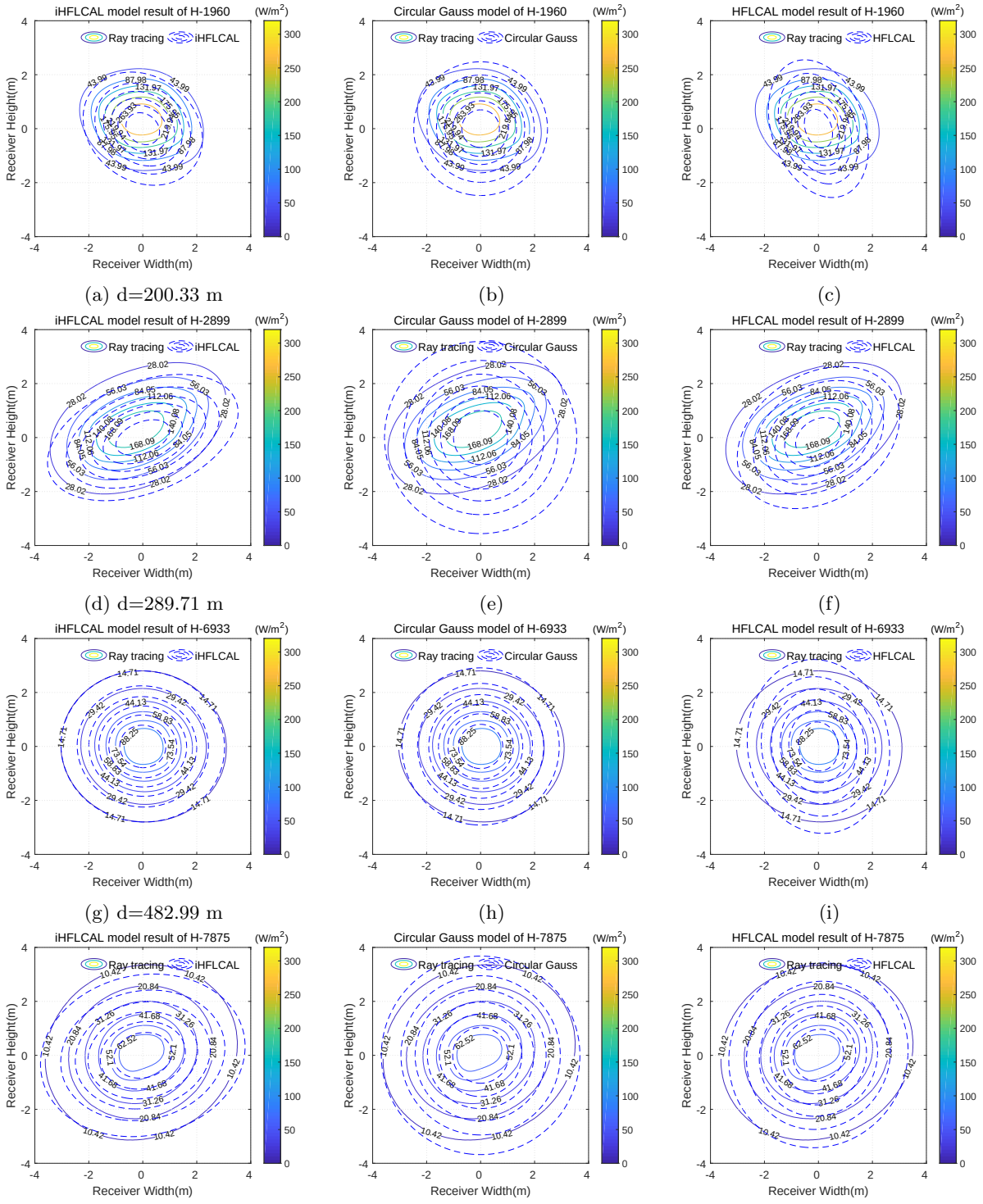

(a) d=200.33 m (b) (c)

(d) d=289.71 m (e) (f)

(g) d=482.99 m (h) (i)

(j) d=554.2 m (k) (l)

Figure 9: Comparison of the simulation results of the proposed iHFLCAL model (left column), the circular Gaussian model (middle column) and the refined HFLCAL model (right column) and in the early morning case. The ray tracing simulation results (solid line) are regarded as the ground truth.

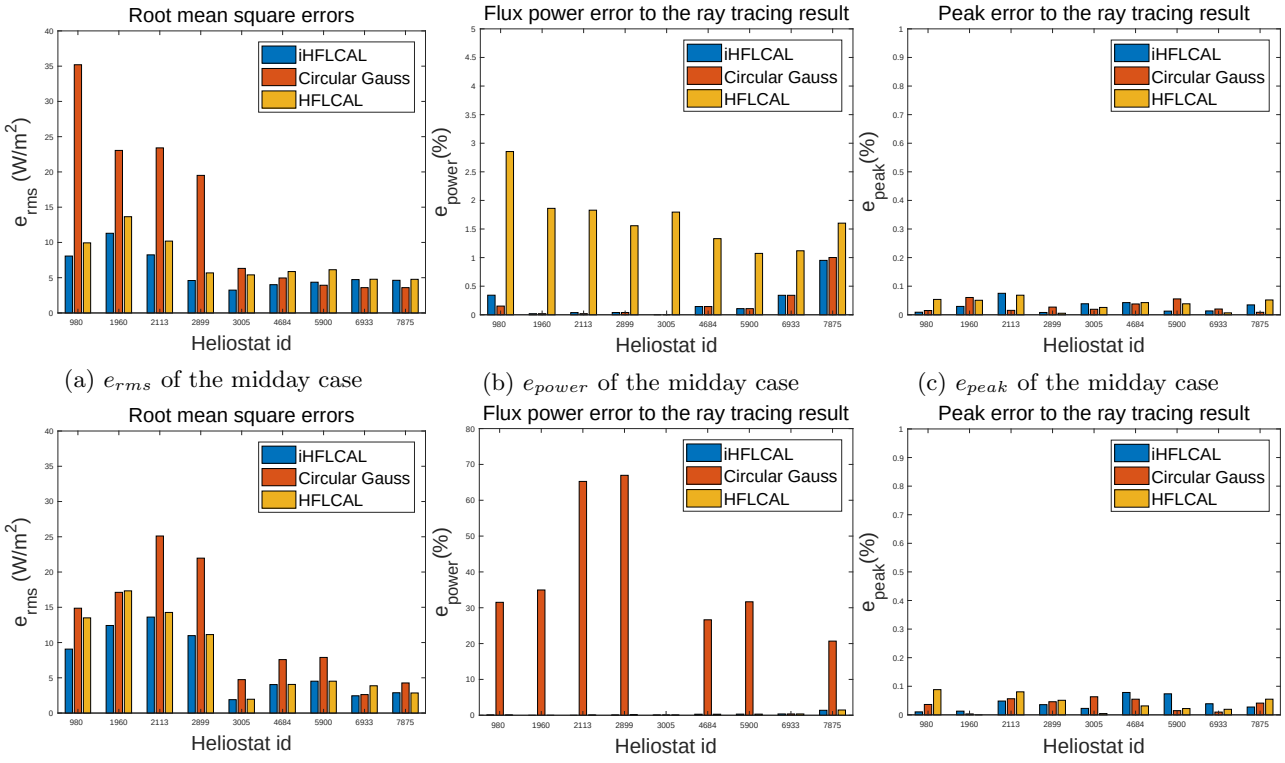

(a) e_{rms} of the midday case (b) e_{power} of the midday case (c) e_{peak} of the midday case

(d) e_{rms} of the early morning case (e) e_{power} of the early morning case (f) e_{peak} of the early morning case

Figure 10: Statistics of the e_{rms}, e_{power}, and e_{peak} of the iHFLCAL model, Gaicía's model and the circular Gaussian model for the midday and early morning cases.

4.3. Comparisons with the Cauchy analytical model

Another comparison is made against the state-of-the-art analytical model, i.e., the convolution-based Cauchy model (He et al., 2019). The simulation and comparison results are presented in Figure 11. Some interesting results were found from the comparison for the convolution-based analytical model and the Gaussian distribution assumption models. First, for the heliostats close to the receiver in the current experiment (approximately less than 300 m), the iHFLCAL model is less accurate than the Cauchy model. Second, the iHFLCAL model works well or even better than the Cauchy model for the heliostats in the middle or far distance, in which the heliostat geometry has weak impact on the flux spot shape, while the sunshape and the slope error of the heliostat become dominate factors for the spot diffusion. Third, the iHFLCAL model can be more efficiently evaluated than the Cauchy model (1.0 ms and 1.4 ms on GPU, respectively) due to its simplified closed-form expression.

4.4. Model discussions

The Gaussian function was originally adopted in the HFLCAL model to approximate the flux spot reflected by a spherically curved heliostat composed of well-canted concentrating mirror facets (Schwarzbözl et al., 2009). In fact, the Gaussian distribution assumption also holds for a flat heliostat (García et al., 2015) for flux prediction purposes, as demonstrated by the experiments in Section 4.1. The iHFLCAL model is versatile to flux simulation of flat mirror facet, which is the fundamental element of a composite focusing heliostat. Two limitations remain in the proposed iHFLCAL model and in the previous HFLCAL models:

- As Schwarzbözl et al. (2009) indicated, the Gaussian model is not suitable for detail description of flux density distributions. The elliptical Gaussian distribution assumption is still not sufficiently accurate

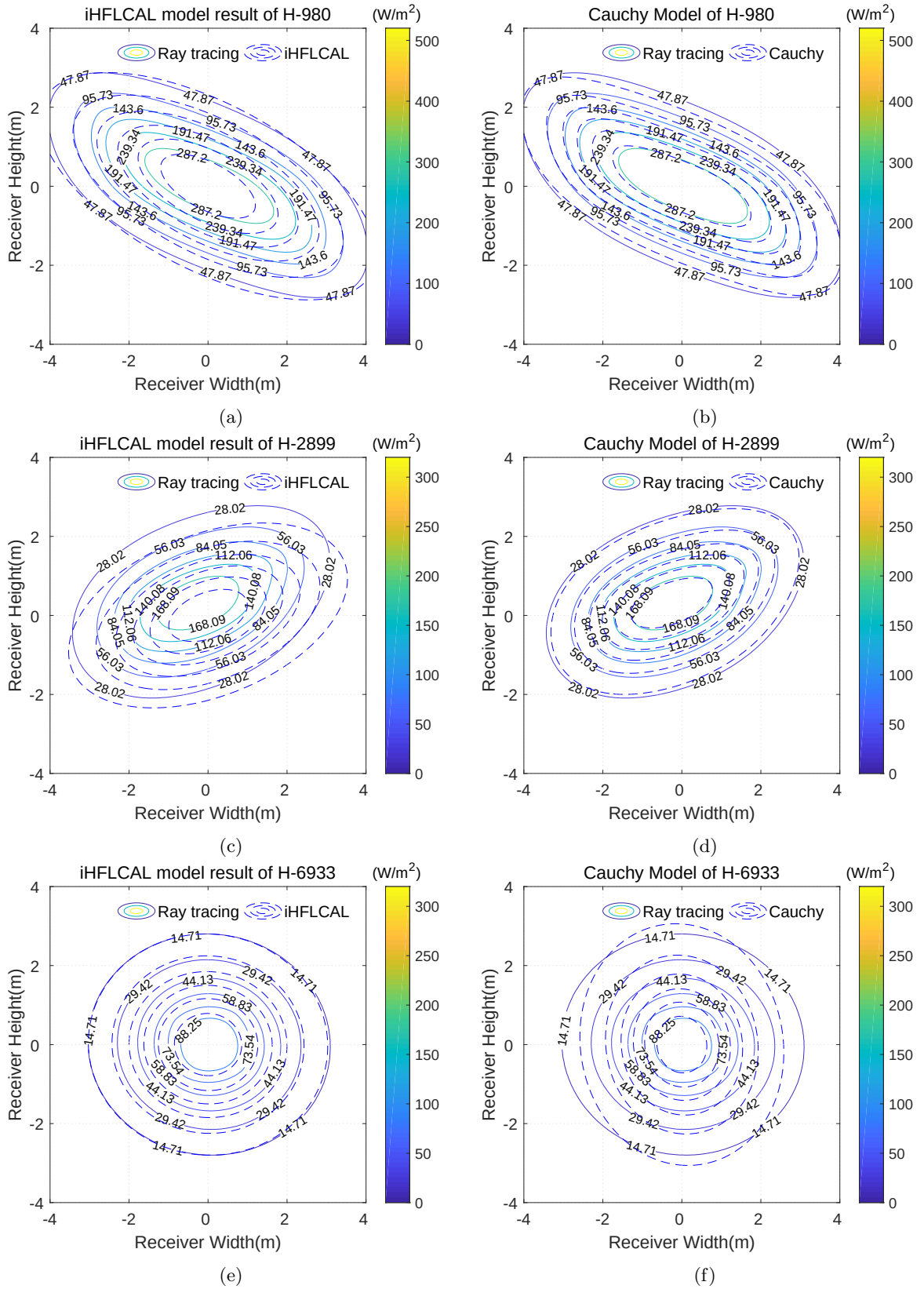

Figure 11: Comparison of the simulation results of the proposed iHFLCAL model (left column) and the convolution-based Cauchy model (right column) in the midday case (a,b) and the early morning case (c∼f).

for the heliostats close to the receiver (Figure 8d; Figure 9d), in which the heliostat size makes the dominant effect and the flux spot is primarily determined by the projection of the heliostat silhouette on the receiver (Elsayed et al., 1995).

- In the proposed iHFLCAL model, shading and blocking effects are accommodated in a straightforward manner by uniformly decreasing the reflected solar flux density distribution according to the actual effective heliostat reflecting surface. Thus, the net power is consistent with the ground truth. However, this treatment remains an approximate one in terms of the flux density distribution (Figure 9; Figure 11).

As a conclusion, the iHFLCAL model obeys the energy conservation principle and achieves more accurate results than the related models based on Gaussian distribution assumption. By establishing new relationship between the standard deviations of the elliptical Gaussian function and the heliostat projected edges, the flux density distributions are better approximated in the iHFLCAL model (Figure 8g; Figure 8i). The model still remains to be not adequately accurate in terms of flux density distribution for some kinds of heliostats. However, due to its high implementing efficiency and accurate flux power prediction, the iHFLCAL model has potential in heliostat field efficiency evaluation and field layout design and optimization.

5. Conclusion

In this paper, the iHFLCAL model with an elliptical Gaussian expression is proposed for modeling the flux spot reflected by a flat heliostat, taking shading and blocking effects into account. The model obeys the energy conservation principle. The factors that have impacts on flux spot are comprehensively analyzed. The flux spots are better approximated by firstly modeling an elliptical Gaussian function on the image plane and then projecting it to the receiver. The relationship between the standard deviations of the elliptical Gaussian function and the heliostat length and width projections on the image plane is explored. Detail analysis and derivation of the flux density distribution function are logically provided step by step. Extensive experiments and comparisons demonstrate that the iHFLCAL model is more accurate than the related Gaussian distribution assumption models. Thus the accuracy of the iHFLCAL model is improved effectively, while its simplicity and conciseness remain unchanged. Since the iHFLCAL model can be evaluated efficiently in parallel on GPU for fast flux simulation of a heliostat, it can be potentially applied in the heliostat field efficiency evaluation, layout and focusing optimizations in future.

Acknowledgments

This work was jointly supported by the National Key Research & Development Program of China (2017YFB0202203) and the National Natural Science Foundation of China (61772464).

Conflicts of interest

There are no conflicts of interest to declare.

References

Besarati, S.M., Goswami, D.Y., Stefanakos, E.K., 2014. Optimal heliostat aiming strategy for uniform distribution of heat flux on the receiver of a solar power tower plant. Energy Conversion and Management 84, 234–243. doi:10.1016/j.enconman.2014.04.030.

Biggs, F., Vittitoe, C.N., 1976. The helios model for the optical behavior of reflecting solar concentrators. Sandia National Laboratories Report Report N0.SAND76-0347 .

Central limit theorem, 2018, . URL: https://en.wikipedia.org/wiki/Central_limit_theorem. [Online; accessed 18-September-2018].

Chen, Y.T., Chong, K.K., Bligh, T.P., Chen, L.C., Yunus, J., Kannan, K.S., Lim, B.H., Lim, C.S., Alias, M.A., Bidin, N., 2001. Non-imaging, focusing heliostat. Solar Energy 71, 155–164. doi:10.1016/s0038-092x(01)00041-x.

Chen, Y.T., Kribus, A., Lim, B.H., Lim, C.S., Chong, K.K., Karni, J., Buck, R., Pfahl, A., Bligh, T.P., 2004. Comparison of two sun tracking methods in the application of a heliostat field. Journal of Solar Energy Engineering 126, 638–644. doi:10.1115/1.1634583.

Closed-form expression, 2019, . URL: https://en.wikipedia.org/wiki/Closed-form_expression. [Online; accessed 15-April-2019].

Collado, F., Gomez, A., Turégano, J., 1986. An analytic function for the flux density due to sunlight reflected from a heliostat. Solar Energy 37, 215–234. doi:10.1016/0038-092X(86)90078-2.

Collado, F.J., 2010. One-point fitting of the flux density produced by a heliostat. Solar Energy 84, 673–684. doi:10.1016/j.solener.2010.01.019.

Cook, R.L., 1982. A reflectance models for computer graphics. ACM Transactions on Graphics 1.

Duan, X., He, C., Zhao, Y., Feng, J., 2019. Quasi-Monte Carlo ray tracing: An efficient and accurate flux density distribution simulation method implemented on a GPU. In preparation. .

Elsayed, M.M., Fathalah, K.A., Al-Rabghi, O.M., 1995. Measurements of solar flux density distribution on a plane receiver due to a flat heliostat. Solar Energy 54, 403–411. doi:10.1016/0038-092X(95)00010-O.

García, L., Burisch, M., Sanchez, M., 2015. Spillage estimation in a heliostats field for solar field optimization. Energy Procedia 69, 1269–1276. doi:10.1016/j.egypro.2015.03.156.

Garcia, P., Ferriere, A., Bezian, J.J., 2008. Codes for solar flux calculation dedicated to central receiver system applications: A comparative review. Solar Energy 82, 189–197. doi:10.1016/j.solener.2007.08.004.

He, C., Duan, X., Zhao, Y., Feng, J., 2019. An analytical flux density distribution model with a closed-form expression for a flat heliostat. Applied Energy 251, 113310. doi:10.1016/j.apenergy.2019.113310.

He, C., Feng, J., Zhao, Y., 2017. Fast flux density distribution simulation of central receiver system on GPU. Solar Energy 144, 424–435. doi:10.1016/j.solener.2017.01.025.

Hennet, J., Abatut, J., 1984. An analytical method for reflected flux density calculations. Solar Energy 32, 357–363. doi:10.1016/0038-092X(84)90279-2.

Huang, W., Yu, L., 2018. Development of a new flux density function for a focusing heliostat. Energy 151, 358–375.

Izygon, M., Armstrong, P., Nilsson, C., Vu, N., 2011. TieSOL–a GPU-based suite of software for central receiver solar power plants, in: Proceedings of SolarPACES, Granada, Spain.

Katzin, M., 1963. The scattering of electromagnetic waves from rough surfaces. Pergamon Press.

Landman, W.A., Grobler, A., Gauch, P., Dinter, F., 2016. Incidence angle effects on circular gaussian flux density distributions for heliostat imaging. Solar Energy 126, 156–167. doi:10.1016/j.solener.2015.12.008.

Leary, P.L., Hankins, J.D., Leary, P.L., Hankins, J.D., 1979. A User's guide for MIRVAL: a computer code for comparing designs of heliostat-receiver optics for central receiver solar power plants. Technical Report Sandia Laboratories Report, Albuquerque, NM, Report No. SAND77-8280.

Lipps, F., Walzel, M., 1978. An analytic evaluation of the flux density due to sunlight reflected from a flat mirror having a polygonal boundary. Solar Energy 21, 113–121. doi:10.1016/0038-092X(78)90038-5.

Lovegrove, K., Stein, W., 2012. Concentrating solar power technology: principles, developments and applications. Elsevier.

Salomé, A., Chhel, F., Flamant, G., Ferrière, A., Thiery, F., 2013. Control of the flux distribution on a solar tower receiver using an optimized aiming point strategy: Application to themis solar tower. Solar Energy 94, 352–366. doi:10.1016/j.solener.2013.02.025.

Schmitz, M., Schwarzbözl, P., Buck, R., Pitz-Paal, R., 2006. Assessment of the potential improvement due to multiple apertures in central receiver systems with secondary concentrators. Solar Energy 80, 111–120. doi:10.1016/j.solener.2005.02.012.

Schwarzbözl, P., Pitz-Paal, R., Schmitz, M., 2009. Visual HFLCAL - a software tool for layout and optimisation of heliostat fields, in: Proceedings of 15th International SolarPACES Symposium, pp. 15–18.

Walzel, M., Lipps, F., Vant-Hull, L., 1977. A solar flux density calculation for a solar tower concentrator using a two-dimensional hermite function expansion. Solar Energy 19, 239–253. doi:10.1016/0038-092X(77)90067-6.

Weiler, K., Atherton, P., 1977. Hidden surface removal using polygon area sorting, in: ACM SIGGRAPH Computer Graphics, ACM. pp. 214–222. doi:10.1145/563858.563896.